Twinning engineering of high-entropy alloys: An exercise in process optimization and modeling

Jongun Moon, Olivier Bouaziz, Hyoung Seop Kim, Yuri Estrin

Version of Record: https://www.sciencedirect.com/science/article/pii/S0921509321009497
Manuscript_e7bf7e9978e823f3e1733d496f2b48c4

Twinning engineering of high-entropy alloys:

An exercise in process optimization and modeling

Jongun Moon[1,2], Olivier Bouaziz[3,4,*], Hyoung Seop Kim[1,2,5,*], Yuri Estrin[6,7]

[1]*Department of Materials Science and Engineering, Pohang University of Science and Technology (POSTECH), Pohang 37673, Republic of Korea*

[2]*Center for High Entropy Alloys, Pohang University of Science and Technology (POSTECH), Pohang 37673, Republic of Korea*

[3]*Laboratoire d'Etude des Microstructures et de Mécanique des Matériaux (LEM3), CNRS, Université de Lorraine, Arts et Métier Paris Tech, F 57000, Metz, France*

[4]*LABoratoire d'EXcellence DAMAS, Université de Lorraine, 57000, Metz, France*

[5]*Graduate Institute for Ferrous Technology, Pohang University of Science and Technology (POSTECH), Pohang 37673, Republic of Korea*

[6]*Department of Materials Science and Engineering, Monash University, Clayton, VIC 3800, Australia*

[7]*Department of Mechanical Engineering, The University of Western Australia, Crawley, WA 6009, Australia*

*Corresponding authors: E-mail address: olivier.bouaziz@univ-lorraine.fr (O. Bouaziz), hskim@postech.ac.kr (H.S. Kim)

Abstract

In a bid to improve the mechanical properties of high-entropy alloys, particularly their strain hardening capability, we adapted the time-proven concept of 'twinning engineering', developed in the context of TWIP steels, to twinning-assisted high-entropy materials. The strategy chosen involved a two-step thermomechanical processing that consisted of low-temperature pre-straining and subsequent annealing. This approach was trialled on CoCrFeMnNi as an exemplary high-entropy alloy. The annealing conditions selected ensured that the deformation twins generated under low-temperature deformation were retained, whilst the dislocation density was recovered. The viability of this strategy was convincingly confirmed for room temperature deformation of the alloy. A constitutive model accounting for the effect of the pre-straining induced deformation twins was proposed. It was shown to provide a reliable description of the low-temperature and room-temperature deformation behavior of CoCrFeMnNi when deformation twins are involved.

Keywords: high-entropy alloys, twinning, recovery, strain hardening, modeling

Introduction

The role of deformation-induced twinning in the mechanical response of face-centered cubic (FCC) metals and alloys is now well established. It is known that deformation twins (DTs) act as strong obstacles to dislocation motion, thus reducing the mean free path of dislocations. This mechanism is often referred to as the dynamic Hall-Petch effect [1, 2]. Most recently, DTs have been utilized to strengthen FCC high-entropy alloys (HEAs) at both room temperature [3-5] and cryogenic temperatures [6-9]. In previous work [10-12], an interesting metallurgical route, which was initially proposed for twinning-induced plasticity (TWIP) steels [13, 14], was applied to enhance the yield strength of an FCC CoCrFeMnNi high-entropy alloy. The specific approach adopted for this HEA involves two steps [12]: (1) pre-straining at 77 K to generate DT and (2) annealing at 500 °C for 1 h to reduce the dislocation density by static recovery. The philosophy behind this treatment was that in this way the material would be provided with strain hardening capability under subsequent deformation. Ideally, the DTs generated at 77 K should be retained. Indeed, it was found [12] that during the static recovery at 500 °C, the DTs remained thermally stable. As a result, the CoCrFeMnNi alloy that underwent this processing schedule exhibited a high yield strength and substantial strain hardening at room temperature, surpassing the conventional grain boundary strengthening [12].

While this processing strategy is promising, there is still a challenging task of optimizating it in order to get the greatest possible benefits in terms of the mechanical performance of HEAs. Looking again at TWIP steels, we note that DTs were found to be thermally stable up to ~625 °C [13]. Notably, Bouaziz *et al.* [13, 14] reported that an excellent combination of yield strength and uniform elongation of TWIP steels was achieved through various processing routes combining cold-rolling and recovery heat treatment. Translating that to the CoCrFeMnNi alloy, one may expect that annealing at a temperature in excess of

500 °C with the aim of recovering stored dislocations, whilst retaining DTs may be promising. It is anticipated that the pre-existing nano-sized deformation twin boundaries generated as a result of the proposed twinning engineering can substantially improve the strength and the strain hardening capability of the CoCrFeMnNi alloy.

In the present study, we attempted to use this kind of 'twinning engineering' for CoCrFeMnNi as a popular exemplar of HEAs. Thermal stability of DTs and the mechanical properties of the alloy with different processing histories were systematically investigated to optimize the heat treatment regime with respect to its tensile properties. A constitutive model describing the microstructural evolution and the associated strain hardening behavior of the CoCrFeMnNi alloy following the thermomechanical treatment identified as an optimum one was also established. The results of the experimental investigation and modeling of the deformation behavior of alloy CoCrFeMnNi are presented below. We will show that the model provides a faithful description of the mechanical behavior of the material after the proposed processing steps. It is thus believed that its use will facilitate design of HEAs with the desired mechanical properties.

Experimental Procedures

An ingot of a $Co_{20}Cr_{20}Fe_{20}Mn_{20}Ni_{20}$ (atomic percent, at%) alloy was cast via vacuum induction melting in an argon atmosphere. The ingot was homogenized at 1100 °C for 6 h in an argon atmosphere, followed by water quenching. To reduce the surface roughness and remove oxides, the homogenized ingot was mechanically milled before cold-rolling. The alloy was cold-rolled from an initial thickness of 7 mm to 1.5 mm. The cold-rolled plate was annealed at 800 °C for 1 h in an argon atmosphere, and then water quenched.

Dog-bone-shaped tensile specimens with a gauge length of 5 mm and a width of 2.5 mm were obtained from the annealed plate. Before the tensile testing, the specimens were polished using SiC papers up to 1,200-grit. Tensile specimens were deformed at 77 K to true strains of 20% and 35% and then annealed at 500 °C, 550 °C, 600 °C, and 650 °C for 1 h in an argon atmosphere, followed by water quenching. After pre-straining at 77 K, the heat treatment was done under different conditions in order to figure out the optimum temperature for recovery heat treatment. After this processing, tensile tests to failure were performed at room temperature. The naming convention of the specimens with different processing histories used in the present work is summarized in Table 1. All tensile tests, including pre-straining at 77 K, were conducted on an Instron 1361 machine at a strain rate of 10^{-3} s^{-1}. An extensometer was attached to the gauge section of each specimen to measure the engineering strain during the tests.

Table 1. The $Co_{20}Cr_{20}Fe_{20}Mn_{20}Ni_{20}$ alloy with the different processing histories.

Processing histories	Naming
Pre-straining to a true strain of 20% at 77 K	P20
Pre-straining to a true strain of 35% at 77 K	P35
Pre-straining to a true strain of 25% at 77 K + recovery heat treatment at 600 °C for 1 h	P20 + A600
Pre-straining to a true strain of 35% at 77 K + recovery heat treatment at 600 °C for 1 h	P35 + A600

Microstructure characterization was performed using optical microscopy (OM) and scanning electron microscopy (SEM) with electron backscatter diffraction (EBSD). For OM, an Olympus BX51M microscope was used. The SEM-EBSD work was done on a JEOL 7800F device. EBSD measurements were conducted using TSL/IM software with a step size of 50 nm. The surface of the alloy for OM was polished up to 1200-grit SiC paper, and then polished by diamond suspensions of 3 μm and 1 μm particle size, followed by etching in an etchant mixed with 45 ml of glycerol, 15 ml of nitric acid, and 30 ml of hydrochloric acid. The surface of the alloy for SEM/EBSD characterization was polished using up to 1200-grit SiC paper, followed by electro-polishing in an etchant solution of 8% perchloric acid.

To measure the dislocation density, X-ray line profile analysis was performed using the convolutional multiple whole profile (CMWP) program. X-ray diffraction (XRD) measurements were conducted using a Bruker D8 Advance equipment. The XRD scans were

carried out with a step size of 0.02° and a holding time of 1 s. The surface of the specimens for XRD measurement was polished with up to 1,200-grit SiC papers.

Results and Discussion

Figures 1(a, b) show the microstructure of the annealed alloy. Its average grain size is 11.54 $\pm$ 4.19 μm. The kernel average misorientation (KAM) map is presented on Fig. 1(b), demonstrates that the alloy is fully recrystallized. The recrystallized fraction was determined using a KAM value of less than 0.5 [15]. Using this standard [15], the procedure returned a value of 95% for the recrystallized fraction. Accordingly, the material was nominally considered as fully recrystallized. The average KAM (KAM_{avg}) value of the annealed alloy is 0.31°. The tensile properties of the annealed alloy at room temperature and 77 K are presented in Fig. 1(c). The yield strength and the ultimate tensile strength of the annealed alloy at room temperature are 309 MPa and 683 MPa, while those at 77 K are 538 MPa and 1,196 MPa, respectively. The uniform elongation of the annealed alloy is 43% at room temperature and 78% at 77 K.

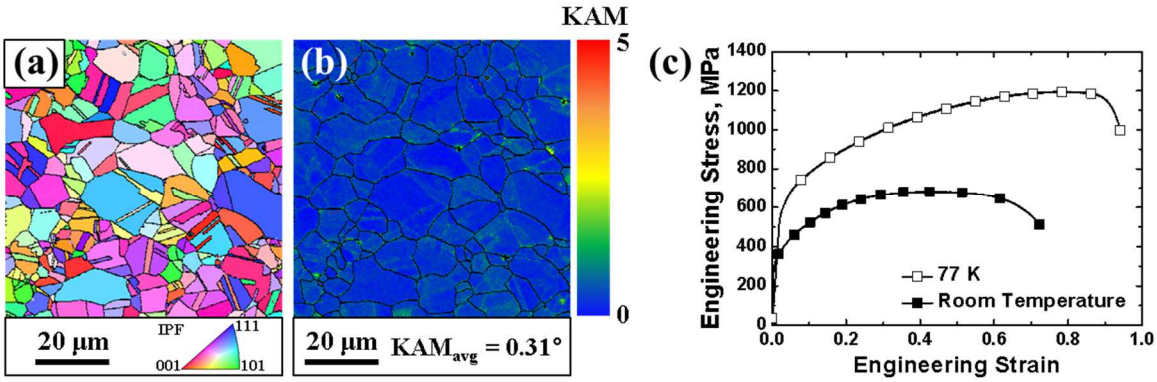

Figure 1. (a) Inverse pole figure and (b) KAM maps for the annealed alloy. (c) Tensile properties of the annealed alloy at room temperature and 77 K.

The microstructure of the alloy after pre-straining at 77 K and subsequent annealing at different temperatures is shown in Fig. 2. Importantly, the coarse-grained structure and the DTs sustain annealing at temperatures up to 600 °C [Figs. 2(a-f)], which indicates that the

alloy has gone through a recovery process. By contrast, the alloy annealed at 650 °C is partially recrystallized, and most of the DTs have disappeared [Figs. 2(g, h)]. Due to the recrystallization, the average grain size of the alloy annealed at 650 °C has dropped to 5.10 ± 2.02 μm [Figs. 2(g, h)]. Thus, it can be considered as proven that the DTs generated by cryogenic deformation in the present CoCrFeMnNi alloy are thermally stable up to 600 °C and lose stability at some temperature between 600 °C and 650 °C. Note that twin boundaries observed in Fig. 2(h) are annealing twin boundaries formed through recrystallization caused by annealing at 650 °C. We shall thus regard the temperature of 600 °C as a notional optimum temperature.

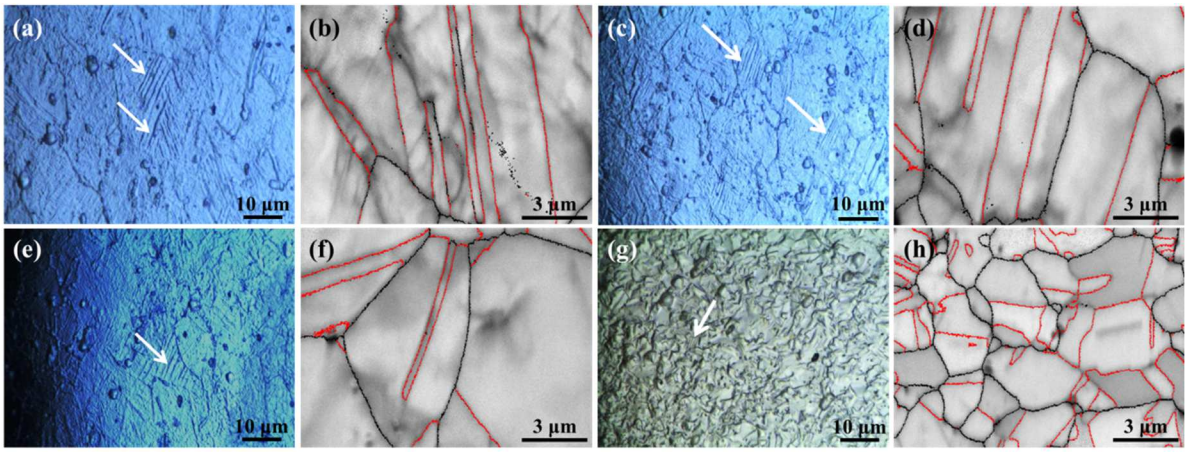

Figure 2. OM images and SEM-EBSD image quality (IQ) maps showing the microstructure of the alloy after pre-straining at 77 K and annealing at (a, b) 500 °C, (c, d) 550 °C, (e, f) 600 °C, and (g, h) 650 °C. The white arrows in (a, c, e, g) point to DTs. The black and red lines in (b, d, f, h) indicate grain and twin boundaries, respectively.

Figure 3 shows the KAM maps with the corresponding distribution plots for the alloy with the different processing histories. As a footprint of the recovery process, the KAM values decrease with rising annealing temperature [Figs. 3(a, b, d, e)]. The corresponding distribution plots also reveal that the pre-strained specimens were successfully recovered after

the annealing [Figs. 3(c, f)]. Notably, the KAM_{avg} values of the pre-strained specimens decline from 1.63° to 0.86° (P20+A600) and from 2.23° to 0.94° (P35+A600) after the recovery heat treatment.

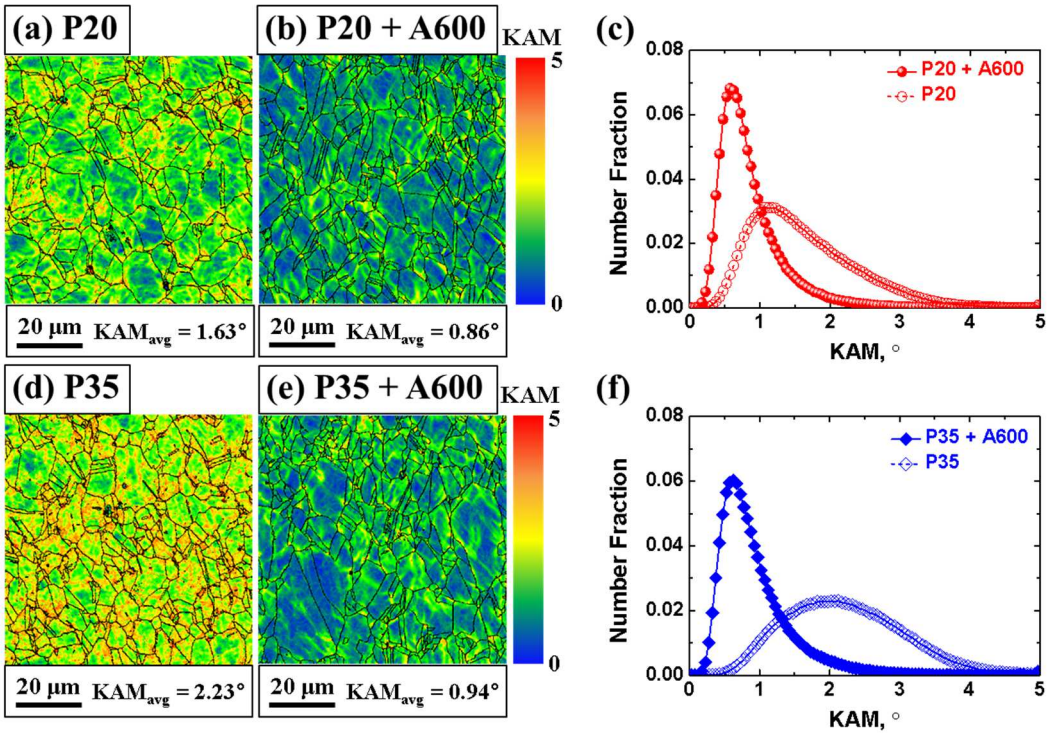

Figure 3. (a, b, d, e) KAM maps and (c, f) the corresponding distribution plots for the KAM values of the pre-strained specimens before and after the recovery heat treatment: (a-c) P20 and P20 + A600 and (d-f) P35 and P35+600.

Mechanical properties at room temperature for the pre-strained and annealed specimens are shown in Fig. 4. It should be noted that the yield strength and the ultimate tensile strength of the alloy were improved appreciably as a result of the present thermomechanical processing [Figs. 4(a, b)]. The yield strength and the ultimate tensile strength rose, respectively, from 309 MPa and 683 MPa in the annealed state to 739 MPa and 924 MPa (P20 + A600) and 949 MPa and 1,040 MPa (P35 + A600) upon the thermomechanical processing according to the two schedules used. Concurrently, the uniform

elongation decreased from 43% (annealed condition) to 21% (P20 + A600) and 14% (P35 + A600). In Fig. 4(c), the true stress vs. true strain curves of the alloy are shifted by the amount of the pre-strain at 77 K. In this representation of the data, it is evident that the pre-strained and subsequently recovered specimens possess higher strength and greater strain hardening capability than the annealed specimens. The increase of the strain hardening rate (SHR) of the pre-strained and then recovered material over that of the annealed one is presented in Fig. 4(d). This demonstrates that the strategy chosen did work: an improved SHR of the alloy was achieved by low-temperature pre-straining followed by annealing at an optimum temperature because the stored dislocations were recovered, whilst the DTs were retained [Fig. 3(b, c, e, f)].

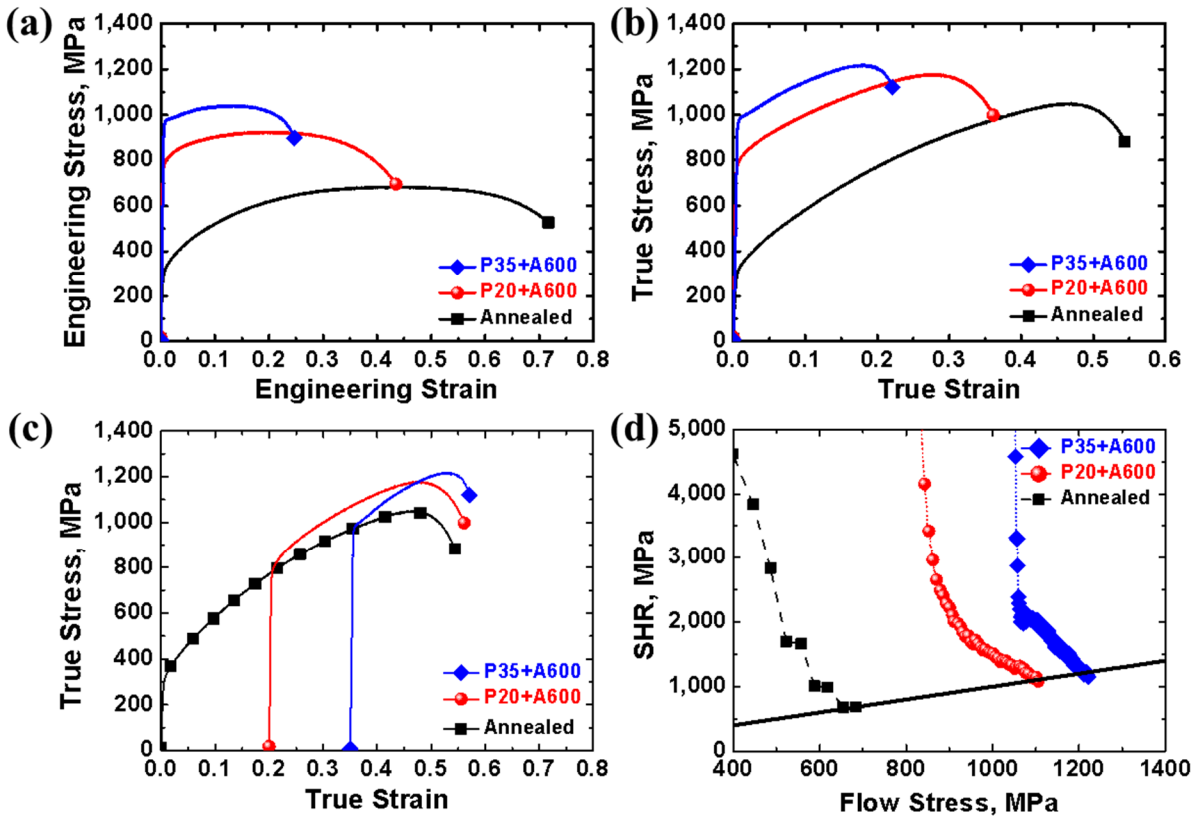

Figure 4. Room-temperature mechanical response of the pre-strained and subsequently recovered specimens: (a) engineering and (b) true stress-strain curves, (c) shifted curves from (b) along the abscissa by the amount of the pre-strain at 77 K, and (d) SHR versus the flow stress of the specimens.

To better elaborate the mechanical behavior of the alloy at room temperature and 77 K, we used a constitutive model adopted from Ref. [16]. As was demonstrated by previous work [16, 17], the model successfully describes the effect of the back stress on the strain hardening of conventional alloys as well as HEAs in terms of the dislocation density evolution. In the model, the flow stress is split into two additive components: one associated with forest dislocations, σ_f, and the other accounting for back stress, σ_b:

$$\sigma = \sigma_f + \sigma_b. \quad (1)$$

It should be noted that σ_f and σ_b are associated with the isotropic and kinematic hardening of the material, respectively [16]. The evolution of the two stress components, σ_f and σ_b, is expressed by the following relations [16]:

$$\frac{d\sigma_f}{d\varepsilon} = \frac{M\alpha\mu bP}{2\sqrt{\rho}} \cdot \frac{d\rho}{d\varepsilon}, \tag{2}$$

$$\frac{d\sigma_b}{d\varepsilon} = \frac{M\alpha\mu b(1-P)}{2\sqrt{\rho}} \cdot \frac{d\rho}{d\varepsilon}, \tag{3}$$

where M is the Taylor factor (M = 3.06 for FCC random texture), α is a constant in the Taylor equation (set at 0.25), b is the magnitude of the dislocation Burgers vector ($b = 2.5 \cdot 10^{-10}\ m$), μ is the shear modulus ($\mu = 81\ GPa$), ε is the applied true strain, and P is a parameter representing the cross-slip probability ($0 \leq P \leq 1$).

According to Eqs. (2) and (3), the variation of both stress contributions are related to the evolution of the dislocation density ρ in the spirit of the Taylor relation. The partitioning into the isotropic and the kinematic hardening components is furnished by the weight factors determined by the cross-slip probability parameter P. Thus, it is the variation of ρ and P that controls the strain hardening during plastic deformation. The evolution of dislocation density is given by a differential equation proposed in [16]:

$$\frac{d\rho}{d\varepsilon} = M\left(\frac{k}{b}\sqrt{\rho}\right) exp\left(-\beta P\sqrt{\rho}\right), \tag{4}$$

where k and β are model parameters. This equation represents the classical Kocks-Mecking evolution equation for stage III strain hardening if $\beta P\sqrt{\rho} \ll 1$. In the opposite limit case, stage IV strain hardening behavior is recovered. As the grain size d affects the dislocation mean free path, the model is modified in the way proposed in [18]:

$$\frac{d\rho}{d\varepsilon} = M\left(\frac{1}{bd} + \frac{k}{b}\sqrt{\rho}\right) exp\left(-\beta P\sqrt{\rho}\right). \tag{5}$$

When deformation-induced twinning occurs, Eq. (5) can be extended to include the effect of twins on the dislocation mean free path [19]:

$$\frac{d\rho}{d\varepsilon} = M\left(\frac{1}{bd} + \frac{1}{bt} + \frac{k}{b}\sqrt{\rho}\right) exp\left(-\beta P\sqrt{\rho}\right), \tag{6}$$

where t is the mean twin spacing. This quantity can be determined from electron microscopy images or computed from the twin volume fraction F and the twin thickness e as [20]:

$$t = 2e\ \frac{(1-F)}{F}. \tag{7}$$

Finally, a closed set of equations is obtained when an evolution equation for the cross-slip probability parameter P is established. To account for the stress dependence of the evolution of P, the following form of this equation can be used [21]:

$$\frac{dP}{1-P} = \frac{\sigma}{\sigma_c} d\varepsilon, \tag{8}$$

where σ_c is the critical stress for cross-slip.

The evolution of the twin volume fraction F with strain ε can be described using an expression proposed in Ref. [22]:

$$F = F_S \frac{m[\exp(\varepsilon(m+l))-1]}{l+mexp(\varepsilon(m+l))}. \quad (9)$$

where F_S is the saturated twin volume fraction (assumed to be 0.1), m is the microstructure-sensitive parameter which depends on stacking fault energy, and l is the rate-controlling parameter for twin production. To estimate t using Eq. (7), we set e to be 13 nm – a value suggested by the observations reported in Ref. [23]. The data on the variation of F during the deformation at 77 K obtained in a previous study [12] was used to fit Eq. (9), as shown in Fig. 5(a). The parameters m and l were determined from the best fit as 0.61 and 4.97, respectively. It should be noted that the model predicts a typical S-shaped curve for the evolution of twin volume fraction in Fig. 5(a). Using Eq. (9), the prediction of twin evolution becomes more accurate than that based on the linear evolution model of twin volume fraction proposed by Olson and Cohen [24] [see Fig. 5(a)]. The R-squared value obtained from Eq. (9) is 0.99, to be compared to 0.96 for the Olson-Cohen model [24]. It is seen that based on this microstructural input [Eq. (9)], the model captures the mechanical behavior of the alloy at 77 K, when profuse twinning occurs [Fig. 5(b)], very well.

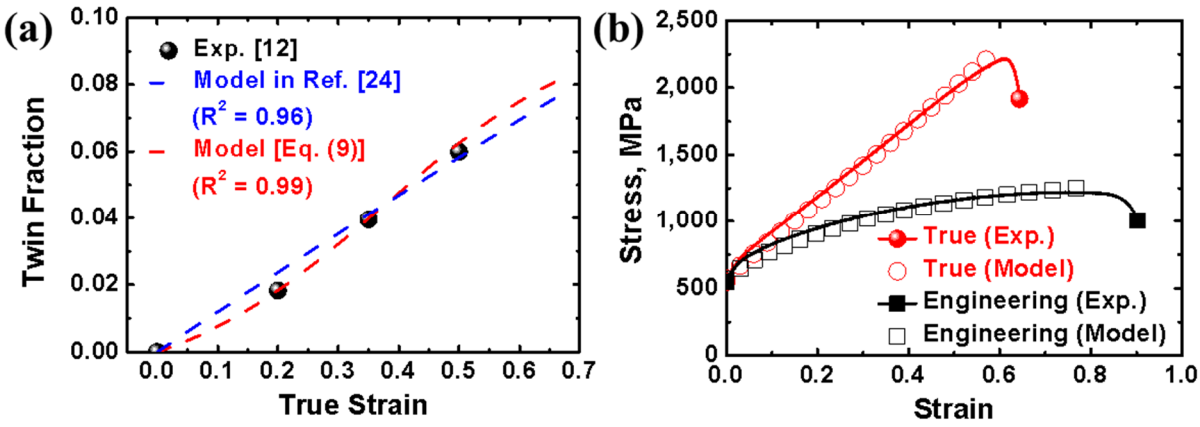

Figure 5. (a) Evolution of twin volume fraction for the annealed alloy (in a state before the thermomechanical processing) during the deformation at 77 K as a function of strain. (b) The true and engineering stress-strain curves for the alloy at 77 K. The acronym 'Exp.' stands for the experimental results.

The evolution of the dislocation density during straining at 77 K can be plotted using Eq. (6) as illustrated in Fig. 6. This variable is crucial as it provides access to the value of the initial dislocation density after the thermomechanical processing conducted in the present work. The measured dislocation density is seen to increase during 77 K-deformation to $3.86 \cdot 10^{15}$ m^{-2} (P20) and $2.03 \cdot 10^{16}$ m^{-2} (P35), while it dropping to $3.25 \cdot 10^{15}$ m^{-2} (P20 + A600) and $1.63 \cdot 10^{16}$ m^{-2} (P35 + A600) after the recovery heat treatment. We note that the measured dislocation density at a true strain of 35% exceeds the model prediction. This may be associated with possible overestimation of the dislocation density obtained from the peak broadening analysis of X-ray diffraction, as other contributions caused by twins, stacking faults, and/or martensite may lead to diffraction peak broadening [25, 26].

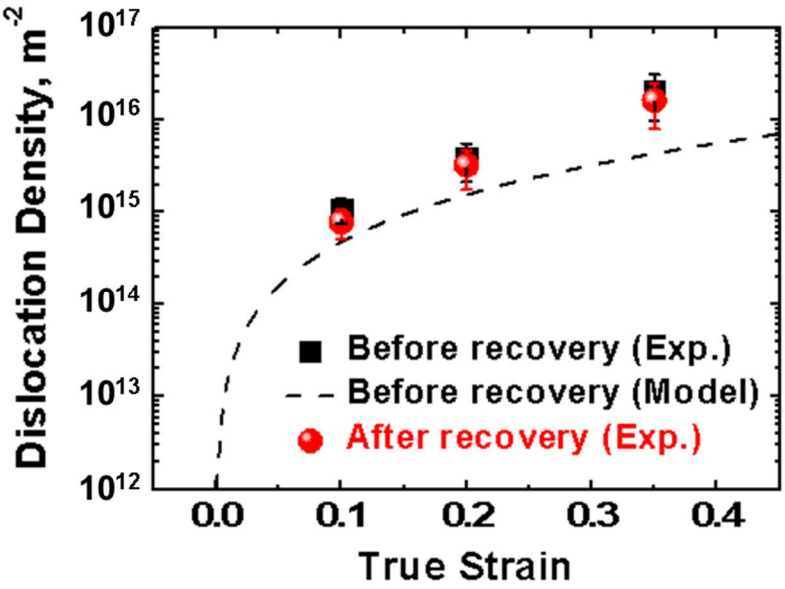

Figure 6. A logarithmic plot of dislocation density evolution with strain in specimens before and after the thermomechanical processing used in the present study. The acronym 'Exp.' stands for the experimental results obtained by measuring the dislocation density by the CMWP method.

Finally, the measured dislocation density attained at the end of the thermomechanical processing at 77 K serves as the input value in the model developed for room-temperature deformation when no deformation twinning occurs. Accordingly, a fixed value for the mean twin spacing *t*, *viz*. that attained at the end of the pre-processing (low-temperature deformation followed by annealing at 600 °C), was used for modelling of room-temperature deformation. It should be noted that the same model parameters were for deformation at room temperature and 77 K (Fig. 5(b)), apart from the initial dislocation density and the mean twin spacing.

The performance of the model can be assessed from Fig. 7, where the experimental deformation curve is presented alongside the calculated one. The agreement between experiment and modeling is judged as very good. This agreement confirms the efficacy of the twinning engineering concept in which twin boundaries contribute to strain hardening at room

temperature by reducing the dislocation mean free path. The modeling shows excellent consistency with the experimental results without any changes in the model parameters regardless of whether the mean twin spacing is variable [Fig. 5(b)] or constant (Fig. 7). This shows that the present modelling accounts for the effect of the DTs retained after the pre-processing on the enhanced strain hardening of the alloy [see Fig. 4(c)].

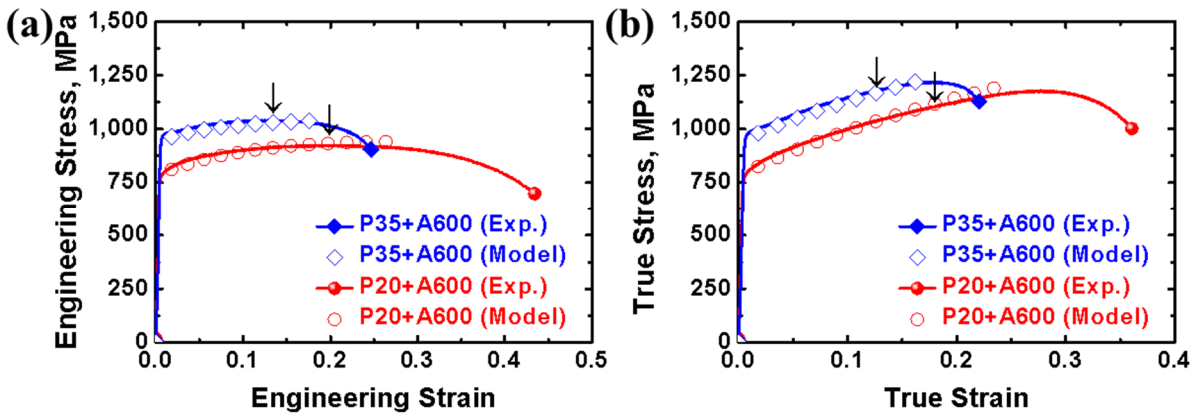

Figure 7. (a) Engineering and (b) true stress vs. true strain curves at room temperature for the present HEA derived from the experiment (Exp.) and the model [Eq. (6)]. The black arrows indicate the end of uniform deformation, i.e., the uniform elongation.

One should note that the twinning engineering can be applied to any material that undergoes deformation twinning. Since the thermal stability of DTs may be different depending on the alloy system, the optimization of the thermomechanical process to sustain DTs and mediate accumulated strain is necessary in order to properly utilize the twinning engineering strategy. We believe that the present exercise in twinning engineering will provide food for thought and further ideas for achieving the improved mechanical performance of TWIP-assisted alloys and HEAs.

Conclusions

In summary, an optimization of two-stage thermomechanical processing of the equiatomic $Co_{20}Cr_{20}Fe_{20}Mn_{20}Ni_{20}$ HEA was carried out to test a twinning engineering strategy for improving the mechanical properties of HEAs. The strategy included generating deformation twins at low temperature (77 K) deformation followed by annealing. The optimization step targeted the selection of the annealing treatment regime achieving excellent mechanical properties. The microstructural evolution of the alloy and its mechanical properties were investigated and interpreted based on the experimental and modeling results. The following conclusions can be drawn:

- Thermal stability of twins induced by deformation at 77 K persisted up to 600 °C. Dislocations were partly recovered at the annealing temperature of 600 °C.
- It was established that deformation-induced twins retained after the recovery heat treatment substantially enhance the yield strength, the ultimate tensile strength, and the strain hardening rate of the alloy at room temperature. The effect is associated with the reduction of the mean free path of dislocations by the retained twins and the capability of the alloy to accumulate the dislocation density from a level diminished by the recovery heat treatment.
- A constitutive model adapted from an earlier version developed initially for TWIP steels was successful in describing the mechanical behavior of the pre-strained and recovered alloy.
- The entirety of the experimental data obtained for the particular alloy studied, supported by the model developed, has demonstrated the viability and potency of the twinning engineering concept proposed. Based on these encouraging results, it can be anticipated that a similar approach can also be applied to a broader range of HEAs.

Acknowledgments

This work was supported by (1) Creative Materials Discovery Program through the National Research Foundation of Korea (NRF) funded by the Ministry of Science and ICT [2016M3D1A1023384], and (2) Basic Science Research Program through the NRF of Korea funded by the Ministry of Education [2021R1A6A3A03044109].

Declarations of Conflict of Interest

None.

Data Availability

The raw/processed data required to reproduce these findings cannot be shared at this time as the data also forms part of an ongoing study.

References

[1] O. Bouaziz, S. Allain, C. P. Scott, P. Cugy, D. Barbier, High manganese austenitic twinning induced plasticity steels: A review of the microstructure properties relationships, *Curr. Opin. Solid State Mater. Sci.* **15** (2011) 141-168.

[2] B. C. De Cooman, O. Kwon, K.-G. Chin, State-of-the-knowledge on TWIP steel, *Mater. Sci. Technol.* **28** (2012), 513-527.

[3] D. Wei, X. Li, J. Jiang, W. Heng, Y. Koizumi, W.-M. Choi, B.-J. Lee, H. S. Kim, H. Kato, A. Chiba, Novel Co-rich high performance twinning-induced plasticity (TWIP) and transformation-induced plasticity (TRIP) high-entropy alloys, *Scripta Mater.* **165** (2019) 39-43.

[4] Y. Deng, C. C. Tasan, K. G. Pradeep, H. Springer, A. Kostka, D. Raabe, Design of a twinning-induced plasticity high entropy alloy, *Acta Mater.* **94** (2015) 124-133.

[5] H. Gasan, A. Ozcan, New eutectic high-entropy alloys based on Co–Cr–Fe–Mo–Ni–Al: Design, characterization and mechanical properties, *Met. Mater. Int.* **26** (2020) 1152-1167.

[6] B. Gludovatz, A. Hohenwarter, D. Catoor, E. H. Chang, E. P. George, R. O. Ritchie, A fracture-resistant high-entropy alloy for cryogenic applications. *Science* **345** (2014) 1153-1158.

[7] Y. Kim, H. K. Park, P. Asghari-Rad, J. Jung, J. Moon, H. S. Kim, Constitutive modeling with critical twinning stress in CoCrFeMnNi high entropy alloy at cryogenic temperature and room temperature, *Met. Mater. Int.* (2020) in press, https://doi.org/10.1007/s12540-020-00818-2.

[8] Y. H. Jo, S. Jung, W. M. Choi, S. S. Sohn, H. S. Kim, B. J. Lee, N. J. Kim, S. Lee, Cryogenic strength improvement by utilizing room-temperature deformation twinning in a partially recrystallized VCrMnFeCoNi high-entropy alloy, *Nat. Commun.* **8** (2017) 15719.

[9] G. T. Lee, J. W. Won, K. R. Lim, M. Kang, H. J. Kwon, Y. S. Na, Y. S. Choi, Effect of microstructural features on the high-cycle fatigue behavior of CoCrFeMnNi high-entropy alloys deformed at room and cryogenic temperatures, *Met. Mater. Int.* **27** (2020) 593-602.

[10] S. J. Sun, Y. Z. Tian, H. R. Lin, S. Lu, H. J. Yang, Z. F. Zhang, Modulating the prestrain history to optimize strength and ductility in CoCrFeMnNi high-entropy alloy, *Scripta Mater.* **163** (2019) 111-115.

[11] S. J. Sun, Y. Z. Tian, H. R. Lin, Z. J. Wang, Z. F. Zhang, Revisiting the role of prestrain history in the mechanical properties of ultrafine-grained CoCrFeMnNi high-entropy alloy, *Mater. Sci. Eng. A* **801** (2021) 140398.

[12] J. Moon, O. Bouaziz, H. S. Kim, Y. Estrin, Twinning engineering of a CoCrFeMnNi high-entropy alloy, *Scripta Mater.* **197** (2021) 113808.

[13] O. Bouaziz, C. P. Scott, G. Petitgand, Nanostructured steel with high work-hardening by the exploitation of the thermal stability of mechanically induced twins, *Scripta Mater.* **60** (2009) 714-716.

[14] O. Bouaziz, D. Barbier, P. Cugy, G. Petigand, Effect of process parameters on a metallurgical route providing nano-structured single phase steel with high work-hardening, *Adv. Eng. Mater.* **14** (2012) 49-51.

[15] C. Moussa, M. Bernacki, R. Besnard, N. Bozzolo, About quantitative EBSD analysis of deformation and recovery substructures in pure Tantalum, *IOP Conf. Ser.: Mater. Sci. Eng.* **89** (2015) 012038.

[16] O. Bouaziz, D. Barbier , J.D. Embury, G. Badinier, An extension of the Kocks–Mecking model of work hardening to include kinematic hardening and its application to solutes in ferrite, *Phil. Mag.* **93** (2013) 247-255.

[17] O. Bouaziz, J. Moon, H. S. Kim, Y. Estrin, Isotropic and kinematic hardening of a high entropy alloy, *Scripta Mater.* **191** (2021) 107-110.

[18] Y. Estrin, H. Mecking, A unified phenomenological description of work hardening and creep based on one-parameter models, *Acta Metall.* **32** (1984) 57-70.

[19] O. Bouaziz, N. Guelton, Modelling of TWIP effect on work-hardening, *Mater. Sci. Eng. A* **319-321** (2001) 246-249.

[20] R. L. Fullman, Measurement of particle sizes in opaque bodies, *Trans. AIME*, **197** (1953) 447-452.

[21] N. Ibrahim, J. D. Embury, The Bauschinger effect in single phase b.c.c. materials, *Mater. Sci. Eng.* **19** (1975) 147-149.

[22] A. Vinogradov, A phenomenological model of deformation twinning kinetics, *Mater. Sci. Eng. A* **803** (2021) 140700.

[23] G. Laplanche, A. Kostka, O. M. Horst, G. Eggeler, E. P. George, Microstructure evolution and critical stress for twinning in the CrMnFeCoNi high-entropy alloy, *Acta Mater.* **118** (2016) 152-163.

[24] G. B. Olson, M. Cohen, Kinetics of strain-induced martensitic nucleation, *Metall. Trans. A* **6** (1975) 791-795.

[25] H. Dittrich, A. Bieniok, Measurement methods | Structural properties: X-Ray and neutron diffraction, in: J. Garche (ed.) *Encyclopedia of electrochemical power sources*, Elsevier, 2019, pp. 718-737.

[26] F. HajyAkbary, J. Sietsma, A. J. Böttger, M. J. Santofimia, An improved X-ray diffraction analysis method to characterize dislocation density in lath martensitic structures, *Mater. Sci. Eng. A* **639** (2015) 208-218.